Characterization of a miniaturized scintillator detector for time-resolved treatment monitoring in HDR-brachytherapy

Mathieu Gonod[1], Miguel Angel Suarez[2], Carlos Chacon Avila[2], Vage Karakhanyan[2], Clément Eustache[2], Julien Crouzilles[3], Samir Laskri[3], Jean-François Vinchant[3], Léone Aubignac[1], Thierry Grosjean[2]

[1]Centre Georges François Leclerc (CGFL) - Dijon, France
[2]FEMTO-ST Institute - Optics Department - UMR 6174 - University of Bourgogne Franche-Comté – CNRS - Besançon, France
[3]SEDI-ATI Fibres Optiques, 8 Rue Jean Mermoz, 91080 Évry-Courcouronnes, France

E-mail: `thierry.grosjean@univ-fcomte.fr, mgonod@cgfl.fr`

Abstract. **Purpose:** HDR brachytherapy combines steep dose gradients in space and time, thereby requiring detectors of high spatial and temporal resolution to perform accurate treatment monitoring. We demonstrate a miniaturized fiber-integrated scintillator detector (MSD) of unmatched compactness which fulfills these conditions.

Methods: The MSD consists of a 0.28 mm large and 0.43 mm long detection cell (Gd_2O_2S:Tb) coupled to a 110-micron outer diameter silica optical fiber. The fiber probe is tested in a phantom using a MicroSelectron 9.1 Ci Ir-192 HDR afterloader. The detection signal is acquired at a rate of 0.08 s with a standard sCMOS camera coupled to a chromatic filter (to cancel spurious Cerenkov signal). The dwell position and time monitoring are analyzed over prostate treatment sequences with dwell times spanning from 0.1 s to 11 s. The dose rate at the probe position is both evaluated from a direct measurement and by reconstruction from the measured dwell position using the AAPM TG-43 formalism. .

Results: A total number of 1384 dwell positions are analyzed. In average, the measured dwell positions differ by 0.023 ± 0.077 mm from planned values over a 6-54 mm source-probe distance range. The standard deviation of the measured dwell positions is below 0.8 mm. 94 % of the 966 dwell positions occurring at a source-probe inter-catheter spacing below 20 mm are successfully identified, with a 100% detection rate for dwell times exceeding 0.5 s. The average deviation to the planned dwell times is of $0.005 +/- 0.060$ s. The instant dose retrieval from dwell position monitoring leads to a relative mismatch to planned values of 0.14 ± 0.7 %.

Conclusion: A miniaturized Gd2O$_2$S:Tb detector coupled to a standard sCMOS camera can be used for time-resolved treatment monitoring in HDR Brachytherapy.

1. Introduction

High dose-rate brachytherapy (HDR-BT) (Crook *et al* 2020, Viswanathan *et al* 2012) delivers high dose of radiation in few fractions to a tumor while sparing the surrounding organs at risk. The prescribed dose is delivered from a stepping radioactive source of high activity which sequentially treats the target volume, thereby involving steep dose gradients in space and time. As a consequence, HDR-BT imposes stringent operational conditions to achieve a treatment delivery that reliably follows the Treatment Planning System (TPS) calculation (Damore *et al* 2020, Kim *et al* 2004, Simnor *et al* 2009, Viswanathan *et al* 2012, Mayadev *et al* 2015, Kertzscher *et al* 2014). Any deviations of the dwell time or position of the source regarding the planned values can lead to serious errors in the dose distribution (Kim *et al* 2004, Pantelis *et al* 2003, Tanderup *et al* 2008, Buus *et al* 2018). Afterloader malfunctions, erroneous source activity, as well as movements of organs or applicators, can also be responsible for wrong dose administration.

To guarantee that a dose distribution is delivered accordingly to expectations, time-resolved in vivo dosimetry (IVD) has been envisioned for time-resolved treatment verification and error detection (Fonseca *et al* 2020, Verhaegen *et al* 2020). Among time-resolved IVD strategies (Fonseca *et al* 2020), scintillating material coupled to an optical fiber has demonstrated performances in the time-resolved monitoring of the dose rate (Lambert *et al* 2006, Lambert *et al* 2007, Therriault *et al* 2011, Therriault *et al* 2013, Linares *et al* 2019, Andersen *et al* 2009, Belley *et al* 2018, Johansen *et al* 2019, Kertzscher *et al* 2011, Jorgensen *et al* 2021a) as well as dwell time and position verification of the stepping source (i.e., source tracking) (Wang *et al* 2014, Guiral *et al* 2016, Johansen *et al* 2018, Linares *et al* 2020, Johansen *et al* 2019, Jorgensen *et al* 2021b), which represent clinically relevant information (Fonseca *et al* 2020).

In the steep spatial and temporal dose gradients of a stepping HDR-BT source, time-resolved IVD faces the challenge of combining high spatial resolution and high readout rate. High spatial resolution limits volume averaging effect near the radioactive source. As an example, the dose rate varies by 18 % across a 1-mm broad detector positioned at 1 cm from the center of an Ir-192 source. This dose rate variation reduces to about 4 % across a 0.24-mm broad detector. At the same time, a readout rate of at least 10 Hz is necessary to identify errors in a treatment with a dwell time as short as 0.1 s. Shrinking the detection volume while increasing readout speed is a challenge as the signal-to-noise ratio (SNR) of the detection process is strongly degraded, leading to higher uncertainties in the treatment monitoring.

The replacement of plastic scintillators by inorganic scintillators (of higher luminescence yield) at the tip of a 0.5-1mm outer diameter plastic fiber allowed for dramatic SNR enhancement in IVD for BT (Wang *et al* 2014, Guiral *et al* 2016,

Andersen *et al* 2009, Johansen *et al* 2018, Belley *et al* 2018, Johansen *et al* 2019, Kertzscher and Beddar 2019, Jorgensen *et al* 2021a). As a result, time-resolved IVD has been recently reported with a detection volume as small as 0.08 mm^3 (0.4 mm large and 0.5 mm long) and at a 20 Hz readout rate(Jorgensen *et al* 2021a). Despite their energy dependence which requires corrections in a direct dose rate measurement (Jorgensen *et al* 2021a), such detectors can lead to accurate estimation of the instant dose via source tracking methods (Guiral *et al* 2016).

As an alternative approach, the concept of a miniaturized scintillator detector (MSD) has been recently introduced from the harnessing of inorganic scintillators to a narrow 125-μm diameter silica fiber with a microfabricated photonic antenna (Suarez *et al* 2019). A MSD with a detection volume as small as 0.016 mm^3 (0.25-mm diameter and 0.48-mm long ellipsoid) has been demonstrated in external beam radiotherapy (Gonod *et al* 2021). The MSD has been shown to overcome the stem effect, and despite its water nonequivalence (both scintillator and fiber), it minimizes electron fluence perturbation due to its extreme compactness.

In this paper, we demonstrate the potential of the MSD concept for source tracking and dose rate monitoring in HDR-BT. Our detector consists of a 0.017 mm^3 detection cell (0.28 mm diameter and 0.43 mm long ellipsoid) attached to the end of a 110-μm diameter silica optical fiber connected to a standard sCMOS camera. After specification of the MSD in terms of SNR, linearity, repeatability and temperature dependence, the detector is calibrated for source tracking. Calibration process is decorrelated from the potential source positioning errors of the afterloader by displacing the detector, rather than the source, with a high precision 2D translation stage. Finally, the MSD is tested in clinical HDR-BT conditions. Dwell position, dwell time and dose rate verification are performed in this study.

2. Material and methods

2.1. Fiber probe

The MSD shown in Fig. 1(a) consists of a 0.017 mm^3 scintillating cell (0.28-mm diameter and 0.43 mm long ovoid) attached to the end of a 110-μm outer diameter (100-μm core diameter) and 2-meter long biocompatible fiber from SEDI-ATI. Prior to scintillator-to-fiber attachment, the fiber tip is specifically tapered to produce a "leaky-wave" photonic antenna (Kraus *et al* 2006, Suarez *et al* 2019) aimed at enhancing the optical coupling efficiency between the scintillating material and the fiber. Terbium-doped gadolinium oxysulfide (Gd$_2$O$_2$S:Tb) is chosen as the scintillator for our MSD. This material is known to emit visible light upon exposure with good efficiency, stability and linearity at room temperature (Qin *et al* 2016, Hu *et al* 2018, Alharbi *et al* 2018). One other advantage of Gd$_2$O$_2$S:Tb is the very low temperature dependence of its luminescence intensity (O'Reilly et al 2020). Gd$_2$O$_2$S:Tb belongs to the family of inorganic (water nonequivalent) scintillators, whose superior X-ray to light conversion efficiency is in favor

of a higher accuracy in IVD, at the expense of an energy dependence of the detector that need to be corrected (Wang *et al* 2014, Guiral *et al* 2016, Andersen *et al* 2009, Johansen *et al* 2018, Belley *et al* 2018, Johansen *et al* 2019, Kertzscher and Beddar 2019, Jorgensen *et al* 2021a). The optical fiber is surrounded by an opaque 0.9 mm black hytrel cladding to be protected from background light of the treatment room. Both the scintillating cell and the last 1.5 cm of the fiber extend beyond the extremity of the opaque cladding to be directly in contact to the phantom.
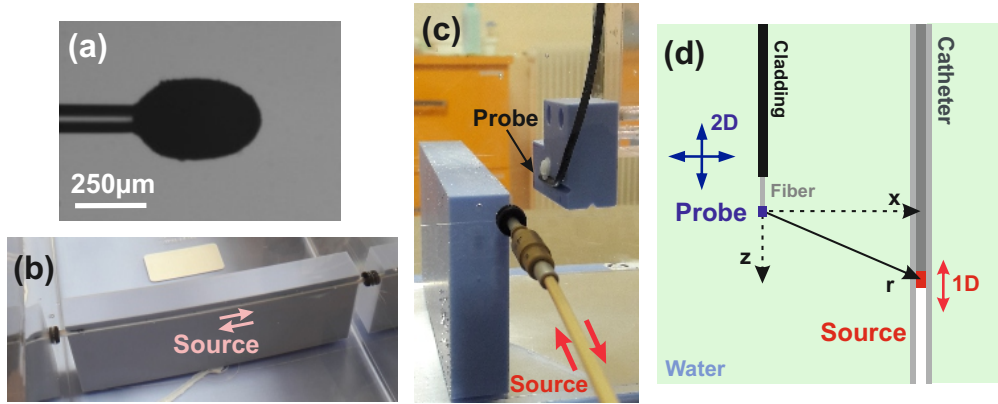

Figure 1. (a) Magnified optical image of the MSD. (b) Photograph of the source catheter in the water tank. The catheter is embedded in a piece of solid water to be maintained straight. (c) Photograph of experimental setup with the detector attached to a holder made with solid water. The holder is movable thanks to a 2D motorized translation stage. (d) Schematic of the irradiation configuration in the water tank, top view.

2.2. Optical readout

The optical signal from the MSD is recorded with a standard sCMOS camera (Zyla model from Andor Technology) whose sensitivity is maximum near the emission wavelength of the scintillators. The camera is placed in the control room, it is connected to the detector via a ten-meter fiber patch cable (with FC/PC connectors). To image the fiber output, the camera is equipped with a 35 mm objective (Fujinon HF35SA) and operates with an integration time of 0.08 s. The camera is driven under Labview in a Windows environment. Each image of the fiber output is automatically integrated over a specific region of interest, leading to an analog 12.5 Hz electric signal directly proportional to the MSD optical signal. Prior to photodetection, the Cerenkov signal present in the fiber upon exposure (the stem effect) is removed with a narrow chromatic filter (544/24 nm band pass filter from Semrock) positioned in front of the camera (Gonod *et al* 2021). We verified that the detected stem effect is negligible in the presence of the chromatic filter, by use of a scintillator-free tapered fiber moving close to the source.

2.3. Brachytherapy system

HDR irradiation is realized with a MicroSelectron afterloader equipped with a 9.1 Ci Ir-192 HDR source. Reference dose rates were calculated using the AAPM-TG43 protocol (Perez *et al* 2012). These reference values are those applied to the TPS.

2.4. Phantom

Irradiations are conducted in a $40\times30\times30$ cm^3 water tank. Two opposite polymetyl methacrylate (PMMA) walls of the tank are perforated to allow the source catheter to cross the tank horizontally (Fig. 1(b)). Tight seals fill the opening between catheter and tank walls to avoid water leakage. To be maintained straight in water, the source catheter is fixed in a V-groove milled in a piece of solid water immersed in the water bath. The water tank ensures a 10 cm scatter material all around the source. No temperature control of the water bath is performed during experiments. Water temperature ranges from 17° to 19° during acquisitions. To realize detector specification and calibration, the end of the fiber probe is mounted onto a solid-water/PMMA holder connected to a high precision 2D translation stage distributed by Thorlabs (Fig.1(c)).

In our experiments, the axes of the source catheter and fiber probe are parallel (Fig. 1(d)). The coordinate frame of the set-up is arbitrarily chosen to be linked to the detector. The origin of the frame coincides with the point-like scintillation cell of the MSD. The z-coordinate of the source is controlled either by the afterloader or one axis of the 2D translation stage used for the probe positioning. The x-coordinate is solely controlled by the second orthogonal axis of the 2D motorized stage.

2.5. Detector specification and calibration

Detector specification and calibration is realized by moving the detector around the radioactive source, which remains static within its catheter. The SNR, dose linearity and repeatability of the detector are assessed with the probe positioned 10 mm away from the source along the (0x)-axis. The linearity of the MSD is tested as a function of the absorbed dose. The repeatability of the MSD is analyzed over ten irradiations of 30 seconds. Between two exposures, the sources is moved back into the afterloader and repositioned near the detector.

To evaluate the energy dependence of the MSD, the probe is scanned over the horizontal (xz)-plane containing the source, with the source maintained at a fixed position within the catheter. During raster scan, an image is accumulated by steps of 2 mm and 1 mm along the (0x) and (0z), respectively, with an integration time at each probe position of 0.16 s. Note that, by virtue of cylindrical symmetry of the source radiation, the dose distribution in the orthogonal (xz) and (yz) planes are expected to be identical. The acquisition procedure starts by positioning the detector at 10 mm from the source. The detector is then moved away from this reference position by 37 mm along (0x) and 32.8 mm along (0z) with the motorized stage. Finally, a raster

scan is launched with the probe progressively approaching the source. The resulting image spreads over 41×66 mm^2, ranging from 6 mm to 47 mm along (0x) and -32.8 mm to 32.8 mm along (0z). The detected optical signal is converted into a dose rate using the conversion rule $D_{exp} = aS + b$, where a and b are constants (Andersen *et al* 2009). The conversion parameters a and b are chosen to minimize the difference between the measured and planned dose rates across the overall acquisition area. The planned dose rate is calculated for all source-probe distances by use of the AAPM TG-43 dose parameters (Perez *et al* 2012).

The detector is calibrated along 5 lines parallel to the (0z)-axis and spaced by 6, 10, 20, 30 and 40 mm from the central axis of the source catheter. To this end, the probe sequentially scans over these lines by 1-mm steps and 125 to 375 images are integrated per probe position. The scan ranges from -55 mm to +5 mm along (0z). An interpolation is then applied to the experimental profiles to achieve a 0.1-mm sampling rate.

2.6. Dwell position, dwell time and dose rate verification

2.6.1. Measurements The MSD is tested using a 22-needle treatment protocol of prostate cancer. In our study, the 22 dose deliveries are realized with the source stepping within the same catheter (Fig. 1(b)). Each treatment sequence relies on a 12-to-16 dwell position protocol based on 2.5 mm steps and dwell times ranging from 0.1 to 11 seconds. The overall treatment is repeated at 5 different spacings x between the source and the probe: 6, 10, 20, 30 and 40 mm (Fig.1(d)). Therefore, for each source-probe spacing x, the source travels 22 times within the same catheter shown in Fig. 1(b). Each of the 22 source displacements within the catheter follows a specific dwell position sequence. Information on the phantom and experimental set-up is detailed in section 2.4.

2.6.2. Dwell position monitoring At each time of the treatment monitoring, the position z of the source along the catheter ($z < 0$) is determined from the readout signal and the source activity using the calibration table of the detector. The source-probe spacing along (0x) being precisely known (with an accuracy of 6.5 μm (Thorlabs Webpage)), the source-probe distance r is deduced from x and $|z|$ (Fig.1(d)). The displacement time of the source between two successive dwell positions being of the order of a few tens of milliseconds (Fonseca *et al* 2015), the resulting rise and fall times in the staircase readout signal are described by one or two acquisition points. To ensure that these transient phases are not included in the dwell position verification, the first and last acquisition points of each dwell position are omitted.

During treatment delivery, the MSD delivers a temporal signal $S(t)$. At each instant $t = k\tau$, where $k \in \mathbb{N}$ and τ is the acquisition time of the camera, the instant source position is deduced from the readout signal S as follows.

First, function f^k is defined as:

$$f^k(z) = \left| C(z) - S^k \right|, \tag{1}$$

where $C(z)$ and S^k are the calibration curve and readout signal at the kth time step, respectively. z is the space coordinate along the source catheter, sampled at 0.1 mm. The stepping source being located only at negative z-coordinates $z < 0$ (the origin of the z-axis is bound to the point-like scintillating cell), function f^k shows a single minimum across the entire range of source positions. The instant source position Z^k then corresponds to the z-coordinate of the minimum of f^k. The source-probe spacing x being precisely known, we can deduce the instant source-probe distance r from Z^k using the formula (cf. Fig. 1(d)):

$$r = \sqrt{x.^2 + |Z^k|^2}, \tag{2}$$

In section 3, dwell position verification will be reported in terms of r and x, rather than x and Z^k). Coordinate Z^k can however be deduced from r and x for each source position using Eq. 2.

2.6.3. Dwell time verification HDR-BT monitoring leads to staircase time traces whose edges delimit two successive dwell positions of the source. Being equal to the delay between two consecutive edges, dwell times can be estimated from edge identification in the detection signal. Convolution techniques (Canny 1986, Guiral *et al* 2016) or signal derivative algorithms (Johansen *et al* 2019) have shown good performances in dwell time verification. Here, we develop an alternative approach which minimizes noise while avoiding time averaging process which can decrease accuracy in dwell time determination. The temporal edges of the staircase signal S are identified using function F defined as:

$$F_i = [S_{i+1} - S_i] \frac{SD_i^N}{\sqrt{S_i}}, \tag{3}$$

where S_i is the ith point of the time trace (i is the ratio between the measurement time and the acquisition rate) and $S_{i+1} - S_i$ is the difference between two consecutive points. SD_i^N is a standard deviation calculated over N consecutive points of the time trace, centered with respect to the ith point. In this study, N is equal to 5. $\sqrt{S_i}$ quantifies the fluctuation of the detected signal due to the camera noise. The shot noise being the main limiting factor of the camera sensitivity (verified in Fig. 3 (d)), these fluctuations can be described by a Poisson statistics where the variance of the detected signal matches the signal intensity. We also have :

$$SD_i^N = \sqrt{1/N \sum_{k=i-(N-1)/2}^{i+(N-1)/2} (S_k - \bar{S})^2}, \tag{4}$$

where

$$\bar{S} = \frac{1}{N} \sum_{k=i-(N-1)/2}^{i+(N-1)/2} S_k, \tag{5}$$

x (mm)	$z = 0$ mm		
	SNR	DTR (%)	LC
6	205	0.49	>0.999
10	147	0.68	>0.999
20	89	1.12	>0.999
30	66	1.52	>0.999
40	52	1.92	>0.999

Table 1. Specification of the MSD at five different values x of the spacing between the source and the probe (cf. Fig. 1(d)). The source and the detector are aligned along the catheter axis (z=0 mm). SNR: Signal-to-Noise Ratio, DTR: Deviation to perfect repeatability (SD), LC: Linearity Coefficient regarding the absorbed dose.

2.7. Dose rate retrieval

The dose rate (D_{meas}) in an individual dwell position is obtained from the measured dwell position and source activity by applying the AAPM TG-43 dose parameters (Perez *et al* 2012). The relative offset to the planned dose rate $\Delta D/D = D_{meas}/D_{TPS} - 1$ is then calculated. D_{TPS} is the planned dose rate for each dwell position of the TPS.

2.8. Uncertainty budget

Following Ref. (ISO,1995), uncertainties are categorized in two types, namely, Type A when data is treated via any valid statistical method, and Type B which involves scientific judgment based on available information. An uncertainty u of Type B is evaluated using the expression : $u = (v_{max} - v_{min})/\sqrt{(12)}$, where v_{max} and v_{min} are the maximum and minimum values, respectively. The combination u_{tot} of a series of uncertainties (u_i, $i \in N$) reads $u_{tot} = \sqrt{\sum_i u_i^2}$.

3. Results

3.1. Detector specification and calibration

The SNR, dose linearity and repeatability of the MSD are analyzed in Table 1. The SNR varies from 205 to 52 at source-probe spacings x of 6 mm and 40 mm, respectively, with a source activity of 9.1 Ci. The linearity coefficient of the MSD exceeds 0.999 for all values of x.

To investigate the energy dependence of the MSD, a 2D field map is plotted near the radioactive source (Fig. 2(a)). This image reveals the steep dose gradient of the source in 2D. From a basic signal-to-dose conversion, we find that our measurement deviates from the expected dose rate by 5.2 ± 4.7 (1SD) % across the scan area, with minimum and maximum discrepancies of 0.006% and 24.8 %, respectively (Fig. 2(b)). Therefore, a direct measurement of the dose rate with our MSD requires space-dependent correction factors.
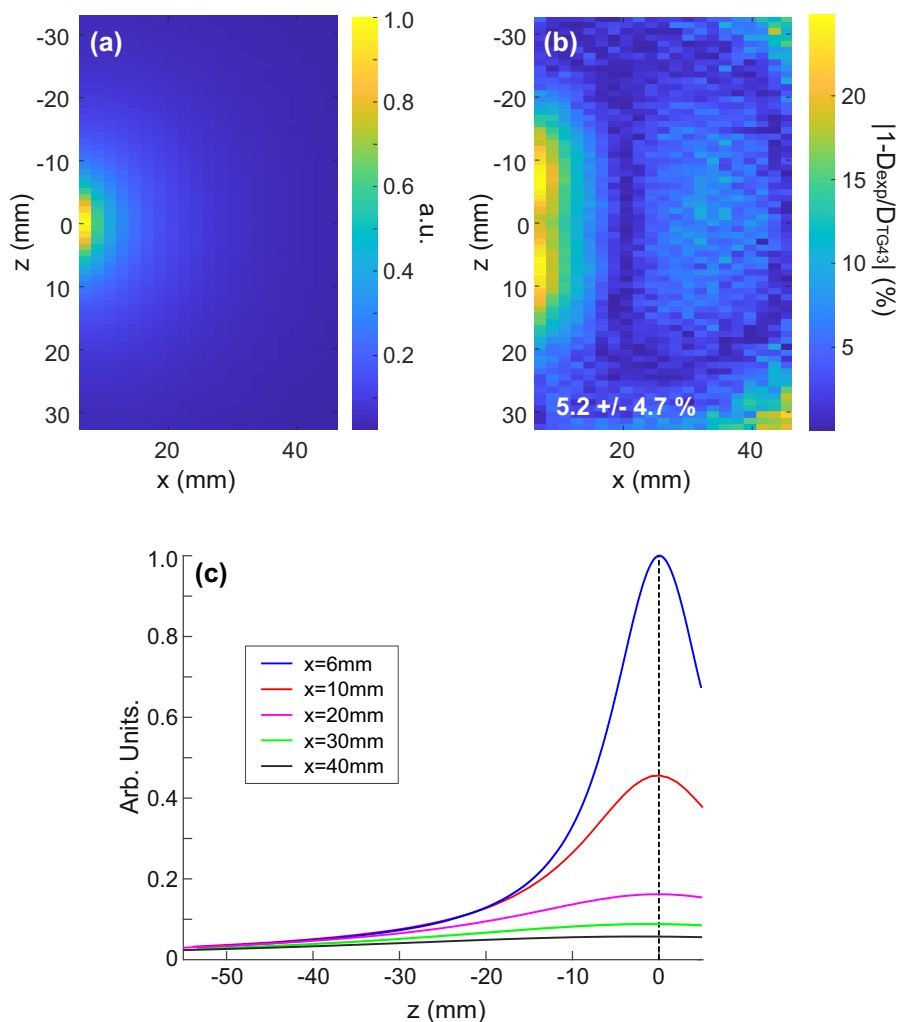
Figure 2. (a) 2D field map acquired with the MSD near the radioactive source. We plot the intensity of the detected optical signal accumulated by our probe during raster scan. (b) Mismatch between the measured and expected dose rates (as a percentage of the expected dose rate). (c) Normalized field profiles plotted at source–probe spacings of 6, 10, 20, 30 and 40 mm. These profiles serve as calibration curves of the MSD for source tracking.

Figure 2(c) shows five radiation profiles along (0z) acquired with the MSD positioned at x equal to 6, 10, 20, 30 and 40 mm. These plots are used as calibration curves of the MSD for source tracking as they provide the signal-to-position conversion required for time-resolved dwell position verification. To ensure a low fluctuation level in these reference plots, the integration time for each probe position of the scan (spaced 1 mm apart from each other) varies from 10 seconds at x=6 mm to 30 seconds at x=40 mm.
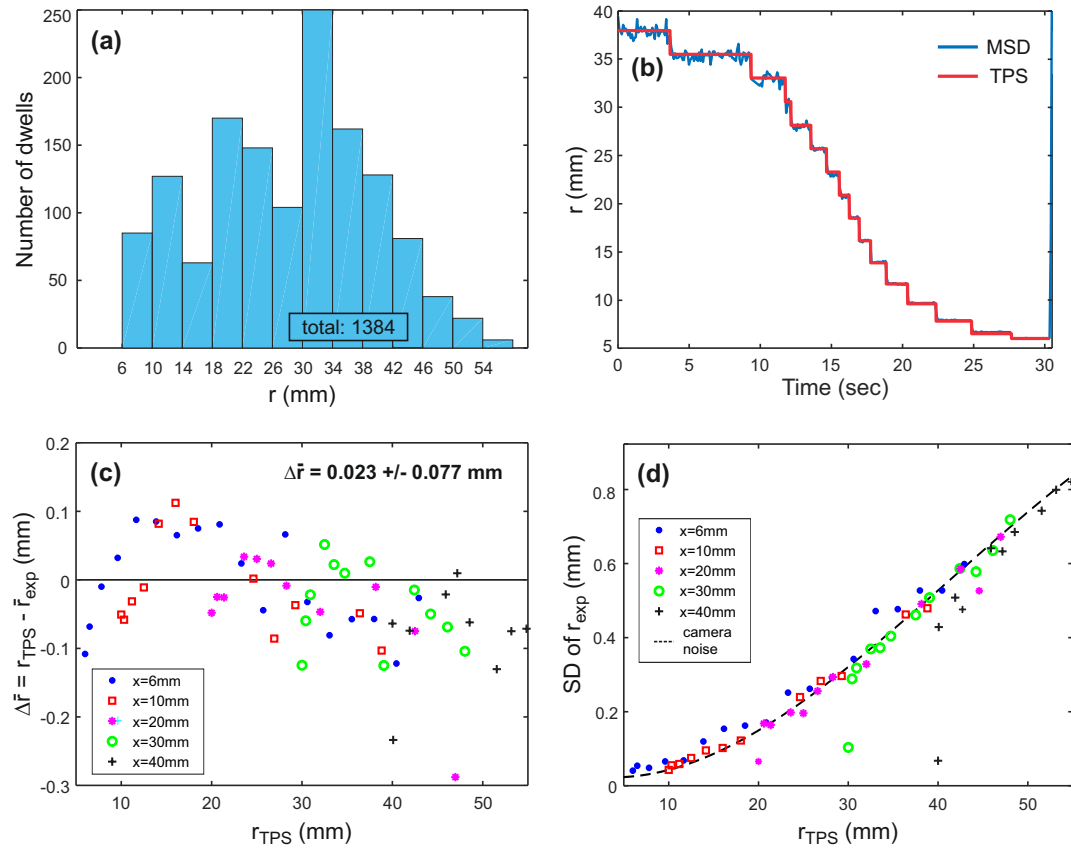
Figure 3. (a) Distribution of the dwell positions across the range of source-probe distances r of our study: number of dwells per distance interval of 4 mm. (b) Measured and planned source-probe distance r versus time for one of the 22 treatment sequences, at a source-probe spacing $x = 6$ mm. (c) Offset between the experimentally determined and planned source-probe distances ($\bar{r}_{exp}$ and r_{TPS}, respectively) as a function of the planned distance r_{TPS}. $\bar{r}_{exp}$ is the average value of the measured distance r over one or more dwell positions. The offset is reported for 5 values of the source-to-probe spacing x (see figure legend). (d) SD of the experimentally determined source-probe distance r_{exp} as a function of the expected distance r_{TPS}. Five values of the source-probe spacing x are considered (see figure legend). Dashed line: theoretical SD of r_{exp} calculated from the predicted noise of the camera.

3.2. Dwell position verification

Our study combines 1384 dwell positions with source-probe distances r (cf. Fig. 1(d)) spanning from 6 to 55 mm. The distribution of dwell positions over the full range of r-values is represented in Fig. 3(a). Fig. 3(b) shows one of the 22 dwell-position sequences of the treatment at a source-probe spacing $x = 6$ mm. We report the experimentally determined source-probe distance r in time, together with the planned values from the TPS.

Fig. 3(c) represents the mismatch to the planned source-probe distances. Each point corresponds to the difference between the planned distance r_{TPS} and the average value $\bar{r}_{exp}$ obtained from measurements over one or more dwell positions. The average

Dwell time (s)	Number of dwells	Identified dwells	Identification rate (%)
0.1	24	0	0
0.2	30	5	17
0.3	36	31	86
0.4	33	30	91
0.5	39	37	95
>0.5	804	804	100
All	**966**	**907**	**94**

Table 2. Identification rate of the dwell positions with the MSD, as a function of the planned dwell time. These results are obtained for source-probe spacings x of 6, 10 and 20 mm.

discrepancy in source-probe distance is of 0.023±0.077 mm (1SD). For each value of r_{TPS}, we also report the SD of r_{exp} (Fig. 3(d)), i.e., the SD of the distribution of instant positions measured at a rate of 0.08s for each planned distance r_{TPS}. We superimpose to these experimental points the theoretical SD curve obtained by converting the predicted shot noise of the camera into distance uncertainty via the calibration curves of Fig. 2(c). The shot noise is statistically described by a variance matching the amplitude of the readout signal (Poisson statistics).

3.3. Dwell time verification

The dwell time verification is performed at source-probe spacings x of 6, 10 and 20 mm, leading to an analysis of 966 dwell positions. The dwell time distribution is reported in Fig. 4(a). The fraction of the dwell times smaller than 1 second, between 1 and 5 seconds, and larger than 5 seconds is of 36%, 59% and 5%, respectively. The identification rate of the dwell positions by the MSD is reported in Table 2. 94% of the dwell positions are identified by the detector. Beyond 0.5 seconds, all dwells are successfully monitored. At the limit of 0.1 second, none are identified. The identification rate increases by a factor about 5 (from 17% to 86 %) when the dwell time increases from 0.2 to 0.3 s. Dwell times of 0.4 and 0.5 s are identified with a rate of 91% and 95%, respectively.

In Fig. 4(c), we plot the difference ΔT between the measured and planned dwell times (T_{exp} and T_{TPS}, respectively). ΔT takes a discrete form imposed by the 0.08-second integration time of the camera. The fourteen values of ΔT that exceeds 0.24 seconds (see the gray regions of Fig. 4(c)) are due to time lags in the data acquisition system, because the camera and data storage are both driven with the same computer (under Windows environment). Lags are evidenced in the time traces by a narrow time window where the noise vanishes and the signal follows a systematic artefactual temporal pattern. When the resulting artefactual points in the figure are removed, the average value of ΔT is statistically calculated to be 0.005 ± 0.060 s (1SD). We see from
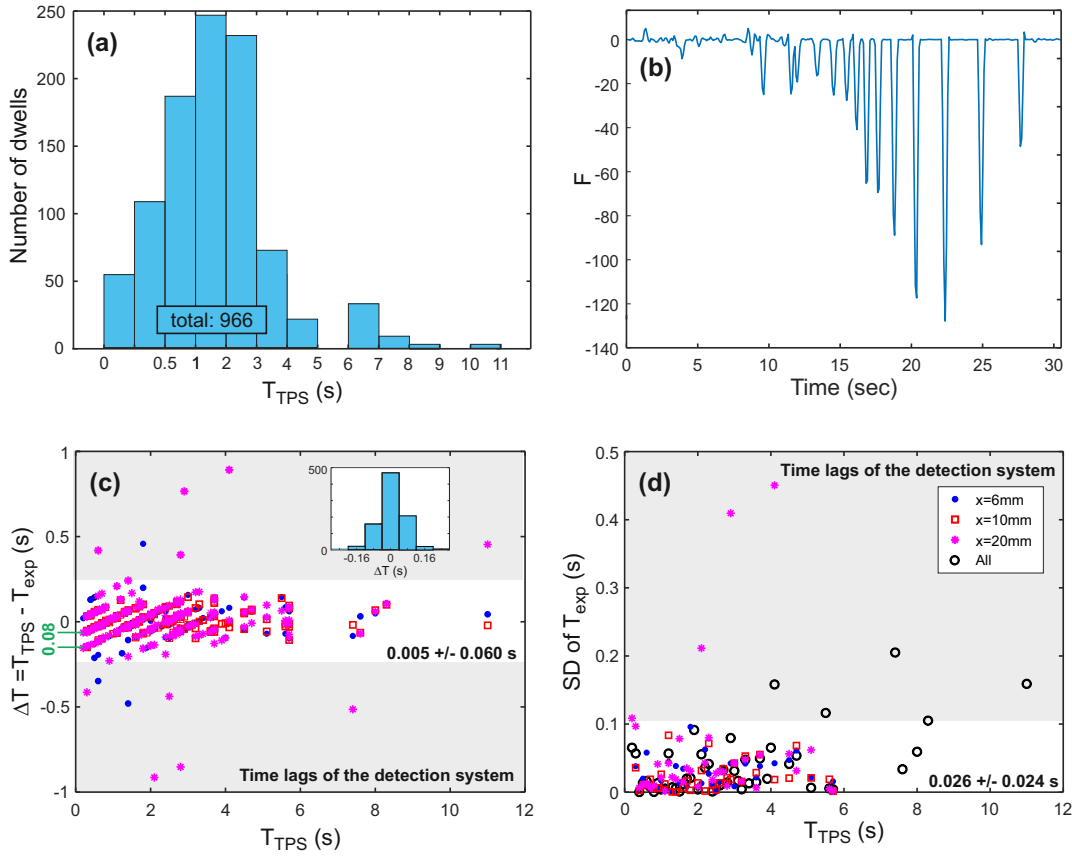
Figure 4. (a) Distribution of the dwell times defined by the TPS: number of dwell positions per one-second time intervals. (b) Temporal-edge detection function F for the treatment shown in Fig 3(b). (c) Offset ΔT between the experimentally determined and expected dwell times (T_{exp} and T_{TPS}, respectively) versus the expected dwell time T_{TPS}. The different shapes and colors of the data points are used to identify the source-probe spacing x, see inset of (d). The fourteen erroneous points located in the gray regions of the figure are due to lags in the data acquisition setup. The statistics of the white central region is calculated after removing these erroneous points. Inset: histogram of ΔT for all 966 dwell positions. (d) SD of T_{exp} as a function of T_{TPS}.

the inset of Fig. 4(c) that 95 % of the identified dwell times are within one integration time of the camera.

Fig. 4(d) reports the SD of T_{exp} versus the planned values T_{TPS}. We calculate the SD of the measured dwell times at each source-probe spacing, and also the average SD for all three spacings. This allows to estimate the uncertainty of the dwell time measurement even if a single dwell position is observed per value of spacing x. The values of the SD that exceed 0.1 s are due to the above-mentioned time lags of the data acquisition system. When these artifacts are filtered out, the SD is found to be of 0.026 $\pm$ 0.024 s (1SD).
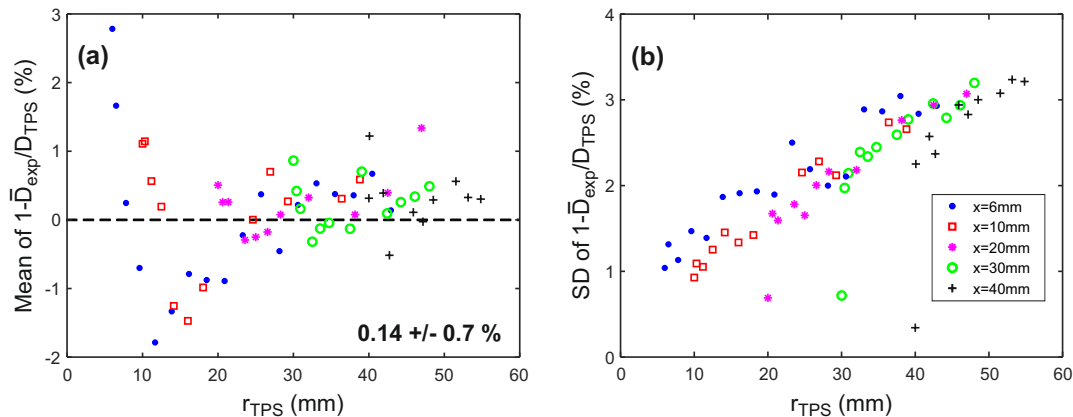
Figure 5. (a) and (b) Average and SD of the relative deviation (in %) between the experimentally determined and planned dose rates ($\bar{D}_{exp}$ and D_{TPS}, respectively), versus r_{TPS}. $\bar{D}_{exp}$ is the average value of the measured dose rate over one or more dwell positions. The offset is reported for the five source-probe spacings x (see legend of (b)).

3.4. Dose rate retrieval

The experimentally determined dose rate per dwell position is reported in Fig. 5. The deviation to the planned dose rates is smaller than 3% across the entire range of source-probe distances. The average error is calculated to be of 0.14 ± 0.7 % (1SD). The larger offsets are observed at the shorter source-probe distances where the dose gradient is maximum. The uncertainty of the dose rate measurement is shown in Fig. 5(b) to be approximately comprised between 1% and 3%.

4. Uncertainty budget

Table 3 provides an uncertainty budget for our study. The positional uncertainty arising from the characterization of the repeatability is defined from Fig. 2(d). The variation of optical signal due to temperature fluctuations of the crystal (in the range of $\pm 1°$) is defined from (O'Reilly *et al* 2020). This temperature-induced signal uncertainty is converted into positional uncertainty using the calibration plots of Fig. 2. Owing to our spectral filtering process, the stem effect is shown to be negligible. With our motorized stage, positional accuracy along (0x) is better than ± 0.01 mm and it has been fixed to ± 0.1 mm along (0z) from our probe-to-source alignment process along the catheter (using this stage). Since the initial positioning of the probe is realized with a ruler, the positioning accuracy of the detector along (0x) by the operator is set to ± 0.5 mm (i.e., half a graduation of the ruler). This contribution only applies to the determination of the dose rate uncertainty.

		x=10 mm, z=-2 mm		x=20 mm, z=-2 mm		Dwell time uncertainty (s)
		Dwell position uncertainty (mm)	Dose rate uncertainty (%)	Dwell position uncertainty (mm)	Dose rate uncertainty (%)	
Detector	Repeatability	0.045 (Type A)	0.197	0.15 (Type A)	0.152	0.058 (±0.1)
	Crystal temp. (±1°C)					
	(0z)	0.058 (±0.1)	0.228	0.289 (±0.5)	0.296	– –
	(0x)	0.012 (±0.02)	0.259	0.023 (±0.04)	0.0264	– –
	Stem effect	0	0	0	0	–
	Integration time	–	–	–	–	0.023 (0–0.08)
	Total	**0.074**	**0.397**	**0.326**	**0.324**	**0.062**
Motorized stage	Position/(0x)	0.006 (±0.01)	0.129	0.006 (±0.01)	0.066	–
	Position/(0z)	0.058 (±0.1)	0.228	0.058 (±0.1)	0.059	–
	Total	**0.058**	**0.265**	**0.058**	**0.089**	**–**
Human	Position/(0x) (± 0.5 mm)	–	6.455	–	3.302	–
Afterloader	Source position/(0z)	0.173 (±0.3)	1.102	0.173 (±0.3)	0.170	**0.058** (±0.1)
Overall		**0.197**	**6.566**	**0.374**	**3.332**	**0.085**

Table 3. Uncertainty budget for the dwell time and position measurements, and the retrieved dose rate.

5. Discussion

5.1. Detector specification and calibration

At a source-probe spacing of 20 mm, our MSD shows a SNR of 89, which is 3.2 times smaller that the SNR reported with the fiber detector of Jorgensen et al (Jorgensen *et al* 2021a) operating at 0.05 s acquisition rate. Assuming optical photometers whose SNR is mainly limited by the shot noise, an operation at 0.08 s of the two detectors would involve a SNR decrease of 4.4 for the MSD. As noted in the introduction, shrinking the detector increases the spatial resolution at the expense of a decrease of the SNR. Our MSD shows a scintillation volume and a cross-section of its fiber core that are reduced by factors of 4.7 and 25 regarding Jorgensen's detector (Jorgensen *et al* 2021a), respectively. In that context, a decrease of the SNR by only 4.4 validates the concept of a nano-optical antenna as scintillator-to-fiber optical interface (Suarez *et al* 2019). To be fully reliable, such a comparison should involve identical photometers for the two probes.

Note that the advantage of miniaturizing a fiber dosimeter is threefold. First, in the steep spatial dose gradients of a HDR-BT source, a smaller sensitive volume reduces volume averaging effect near the source. As an example, the dose rate varies by 7.6 % across a 0.4-mm broad detector (cf. Jorgensen *et al* 2021a) positioned at 1 cm from the center of an Ir-192 source. This dose rate variation reduces to about 4 % across our 0.24 mm broad detection cell. Second, when using inorganic scintillators as a probe, a smaller sensitive volume reduces the electron fluence perturbation, which minimizes the perturbation of the therapeutic process. Finally, shrinking the overall detector (scintillation + fiber) opens the prospect of a new multiprobe architecture in an individual catheter or needle. As an alternative to Therriault's approach (Therriault *et al* 2013), multipoint detectors would be obtained by cascading along (0z) the various probes engineered at the end of a fiber bundle. These multiprobe detectors would be completely free from cross-talk between the detection channels. With the detector approach proposed by Jorgensen et al. (Jorgensen *et al* 2021a), such multiprobe architectures would be too large to be inserted in a BT catheter or a BT needle.

The linearity of the MSD is excellent and agrees well with preceding studies of Gd_2O_2S:Tb-based fiber dosimeters used for monitoring external beam radiotherapy (Qin*et al* 2016, Alharbi*et al* 2018, Hu*et al* 2018, Gonod*et al* 2021). Note from O'Reilly et al (O'Reilly*et al* 2020) that under fixed irradiation conditions, Gd_2O_2S:Tb detectors do not display any significant intensity variations at temperatures ranging from 15 to 40 °C. The Gd_2O_2S:Tb fiber detectors are thus promising candidate for in vivo dosimetry, showing no significant signal variations from room to body temperature.

5.2. Dwell position verification

The average discrepancy to the planned source-probe distances is of 0.023±0.077 mmAs a comparison, Guiral et al. (Guiral *et al* 2016) reported a value of 0.11±0.7 mm over 900 dwell positions in a water phantom. In their detection system, four inorganic scintillator detectors based on 0.36 mm³ scintillation cell were connected to four photomultiplier tubes operating in photon counting regime at a rate of 0.1 second. Despite a 21-fold smaller scintillation volume and the use of a standard camera of lower detection efficiency, the measurement accuracy is significantly better with the MSD.

The standard deviation of our dwell position measurements remains below 0.8 mm over the full range of source-probe distances of this study (Fig. 3(d)). Johansen et al. (Johansen *et al* 2018) reported a standard deviation in between 2 mm and 3 mm over 3239 dwell positions distributed in a similar range of source-probe distances. The detection system involved a fiber-coupled Al_2O_3:C crystal and a photomultiplier tube of larger sensitivity than our standard camera. In the case of Johansen et al. (Johansen *et al* 2018), measurements were realized in vivo during prostate HDR-BT, which may tend to diminish positioning accuracy regarding our highly controlled measurements conducted in a water phantom. Moreover, their analysis focused on dwell times longer than 0.7 s. The ability of their system to monitor source position over short dwell times

could not be assessed.

Figure 3(d) shows that the sensitivity of our camera is the main limiting factor of the dwell position verification. The accuracy of the dwell position monitoring could be increased by use of a photomultiplier tube or an avalanche photodiode, which provide higher SNR capability than a sCMOS camera. However, these highly sensitive photometers are more expensive, can involve kV supply voltage and their detection performances can be seriously degraded after misuses, which are likely with end-users that are non-specialists in optics. By improving in-fiber coupling of the scintillation with a concept of nano-optical antenna (Suarez *et al* 2019), we show that state-of-the-art dwell position verification in HDR-BT is achievable with a standard photometer that is more compatible with clinical protocols.

5.3. Dwell time verification

With a 100% identification rate of the dwell times longer than 0.5 s, the proposed detection system shows promising perspectives for dwell time verification. The performances detailed in Table I are demonstrated over a 40-mm broad and 40-mm long cylindrical measurement volume around the probe axis. Such a volume encompasses the full range of source-probe distances considered in vaginal HDR-BT (typically, $x < 20$ mm and $z < 40$mm) (Belley *et al* 2018). If a larger measurement range is needed, e.g. for covering the maximum treatment volume in prostate HDR-BT (a 60 mm cubic volume), a photomultiplier tube or an avalanche photodiode, rather than a standard camera, could be used to enhance the SNR of the detection system. We however prefer to avoid this detection strategy which is less suitable for a clinical use. An alternative approach would consist of increasing the scintillation volume while keeping a standard camera for the luminescence detection. In that case, problem of volume averaging as well as a perturbation of the therapeutic process may arise. This solution would thus need further investigations to be validated. Finally, multiple miniaturized fiber probes could be inserted in the treatment region. By using four MSD in four dedicated catheters spaced 40 mm apart, one could ensure the performances shown in Table 2 across a 80×80 mm^2 area in the (x,y)-plane perpendicular to the catheter axes. Guiral et al (Guiral *et al* 2016) showed the feasability of a four-probe system and reported the ability with this architecture to extend the source tracking to x and y coordinates. The use of a multiprobe configuration in an individual catheter, as first suggested by Therriault et al. (Therriault *et al* 2013), may also extend the monitoring capability along the (0z)-axis (i.e., the catheter axis). In our case however, the multipoint detector would be obtained by cascading along (0z) the different probes engineered at the end of a fiber bundle. As an example, a fiber bundle of 7 fibers being only 0.375 mm in diameter with our approach, the resulting multiprobe would be narrow enough to be inserted in a catheter.

Dwell time verification is also a matter of edge detection in a staircase signal. Based on a signal averaging, the algorithm developed by Johansen et al. (Johansen *et al* 2019) allows for efficient noise filtering but it lessens the slope of the edge between two

successive dwell positions, thereby reducing the identification probability of the shorter dwell times. Their resulting identification rate, which was of 89 % for dwell times longer than 1 s, dropped down to 25 % for shorter dwell times. We find that 100 % and 83% of the dwell times longer and shorter than 1 s are identified. This could be partly explained by our algorithm which does not affect the edge slope (Fig. 4(b)), at the expense of a lower noise filtering potentially leading to edge-detection limitations for the larger source-probe distances. Edge-detection algorithms based on artificial intelligence could extend the dwell time monitoring capability further away from the probe while keeping time edges unaffected in the data post-treatment.

To overcome lag problems, the camera and data recording should be independently driven by two different systems, such as a micro-controller or a FPGA for the camera and a computer for the data recording. When the artefactual points are filtered out, the SD of the distribution of measured dwell times reduces to 0.06 s, which matches the SD obtained by Johansen et al. (Johansen *et al* 2019). Guiral et al. obtained standard deviations of 0.09 s and 0.08 s with four-detector architectures embedded in a plastic phantom and in an applicator, respectively (Guiral *et al* 2016). With their imaging panel, Fonseca et al. reported a maximum absolute deviation of 0.2 s in a water phantom (Fonseca *et al* 2017). Note that Guiral et al. and Fonseca et al. limited their study to dwell times of the order of 5 s and 10 s, respectively. The performances of their systems to monitor sub-1s dwell times could not be assessed. Johansen et al. performed in vivo monitoring of dwell times shorter and longer than 1s in patient treatments. Reaching similar accuracy with a MSD coupled to a standard camera validates our miniaturization approach. Our MSD indeed shows a 32-fold smaller scintillation cell coupled to a fiber whose waveguiding area is 25 times tighter. Moreover, the inter-dwell spacing is of 3 mm for Johansen et al. and only 2.5 mm in our study, leading to noticeably smaller edges in our case given the steep dose gradients in play.

The good repeatability of our measurements is confirmed in Fig. 4(d) as the SD for all dwell time measurements remain below 0.1 s. The values larger than 0.1 s are due to the time lags of the detection system. As another indicator of the temporal accuracy of our MSD, 95 % of the identified dwell times are within one integration time of the camera (0.08s). Johansen et al. (Johansen *et al* 2019) reported that 97% of the measured dwell times of patient treatments (prostate cancer) were within one sampling point of 0.15 s. In the monitoring of prostate treatment with a flat panel detector, Smith et al. obtained 29 % (78 %, respectively) of the dwell times matching the planned values within one (two, respectively) integration time of their system (0.067 s; 0.13 s, respectively) (Smith *et al* 2018).

5.4. Dose rate retrieval

Relying on water nonequivalent scintillators, our MSD requires a space-dependent correction factor to accurately determine the dose rate (see Fig. 2(b)). The dose rate determination from dwell position (using AAPM TG-43 dose parameters) is more

accurate by one order of magnitude than a direct dose rate measurement (Fig. 5(a)). This indirect approach can be seen to bring the required correction factors. The increase of dose rate offset (up to 3%) at the smaller source-probe distances is due to the steeper spatial gradients of the dose rate close to the source, leading to higher uncertainties in the dose rate determination process. This error level is however 8 times below the discrepancy observed at the same distance range from a direct measurement (Fig. 2(b)). The SD of the distribution of experimental points being smaller than 3% over the full range of source-probe distances (Fig. 5(b)), the time-resolved dosimetry performances of the MSD are fully compatible with IVD for HDR-BT.

5.5. Clinical prospects of the MSD

Our MSD is compatible with clinical applications as it is made of biocompatible materials and it is compact enough to be easily inserted in a catheter, a BT applicator or a BT needle. As a preliminary step, we successfully positioned a MSD at the center of a 1-mm diameter sealed encapsulation tube of biocompatible PEEK material.

Note that the use of a motorized stage to position the probe ensures an accurate assessment of the intrinsic performances of the probe by minimizing manipulation errors. For future clinical use in HDR BT, we will follow the fiber-based treatment verification approaches already proposed in gynecologic BT (Belley *et al* 2018) and prostate BT (Johansen *et al* 2018). In gynecologic BT, the source and the probe can be inserted in two different catheters which belong to the same applicator. In that case, the source-probe spacing x can be precisely known, as in the present study. In prostate BT, the problem is more complex as the source and probe are inserted in different independent needles that are manually implanted in the patient. In that case, the x and z coordinates (see Fig. 1(d)) can become noticeably coupled since the needle implant are rarely perfectly parallel, due to operational errors. In that case, the detection strategy suggested by Johansen et al (Johansen *et al* 2018) is particularly interesting as it enables to find from IVD both x and z coordinates of the source relatively to the probe. 3D positioning strategies by triangulation in a multiprobe architecture may also be an alternative solution.

6. Conclusion

In this phantom-based study, we have demonstrated an IVD system for HDR-BT based on a miniaturized scintillator dosimeter (with high-Z Gd_2O_2S:Tb scintillators) coupled to a standard sCMOS camera. Given its high level of miniaturization and high detection efficiency, such a detector combines high spatial resolution, high detection speed, and low perturbation of the therapeutic process even with inorganic water nonequivalent materials. The use of a standard camera, instead of a photomultiplier tube or an avalanche photodiode of higher sensitivity, is motivated by its better scalability for clinical use. The lower SNR of these photometers is compensated by the concept of

a MSD relying on an interface in between the scintillators and the fiber aimed at improving in-fiber collection efficiency of the X-ray-induced luminescence. Our MSD shows excellent linearity and repeatability and prior studies have reported a negligible temperature dependence of $Gd_2O_2S:Tb$ in the context of a medical application (O'Rreilly *et al* 2020). The average offset to the planned dwell positions is of 0.023 ± 0.077 mm over 1384 dwell positions distributed within the source-probe distance range of 6-54 mm. The standard deviation of the measured source-probe distances varies from 0.04 mm at 6 mm to 0.8 mm at 54 mm. 94 % of the 966 dwell positions at or below the source-probe spacing $x = 20$ mm are successfully identified with a 100% detection rate for dwell times exceeding 0.5 s. 95 % of the identified dwell times are measured with an accuracy of one acquisition time of the camera (0.08 s). The average offset to the planned dwell times is of 0.005 +/- 0.060 s, over values ranging from 0.2 s to 11 s (dwell times of 0.1 s have not been identified with our 0.08 s detection rate). The standard deviation of the measurements for each planned dwell time does not exceed 0.1 s. The dose rate retrieval at the probe position from the dwell position monitoring (using the AAPM TG-43 formalism) leads to an average relative error between experimental and planned values of 0.14 ± 0.7 %, with a standard deviation ranging from 1% to 3% from 6 to 54 mm source-probe distances. Our detector of unmatched compactness is thus totally adequate for IVD in HDR-BT. Future effort will be focused on multiprobe architectures to broaden the monitoring volume and extend source tracking to the three space dimensions (Guiral *et al* 2016). The use of a camera, instead of a single pixel photodiode or a photomultiplier tube, is well adapted to the simultaneous parallel detection required in a multiprobe architecture. Time-resolved treatment monitoring in a patient is also a future goal to assess performances of our detector in IVD.

Acknowledgments

References

Alharbi, M., Gillespie, S., Woulfe, P., McCavana, P., O'Keeffe, S. & Foley, M. (2018). Dosimetric characterization of an inorganic optical fiber sensor for external beam radiation therapy, *IEEE Sens. J.* **19**(6): 2140–2147.

Andersen, C. E., Nielsen, S. K., Greilich, S., Helt-Hansen, J., Lindegaard, J. C. & Tanderup, K. (2009). Characterization of a fiber-coupled luminescence dosimetry system for online in vivo dose verification during brachytherapy, *Med. Phys.* **36**(3): 708–718.

Belley, M. D., Craciunescu, O., Chang, Z., Langloss, B. W., Stanton, I. N., Yoshizumi, T. T., Therien, M. J. & Chino, J. P. (2018). Real-time dose-rate monitoring with gynecologic brachytherapy: Results of an initial clinical trial, *Brachytherapy* **17**(6): 1023–1029.

Buus, S., Lizondo, M., Hokland, S., Rylander, S., Pedersen, E. M., Tanderup, K. & Bentzen, L. (2018). Needle migration and dosimetric impact in high-dose-rate brachytherapy for prostate cancer evaluated by repeated mri, *Brachytherapy* **17**(1): 50–58.

Canny, J. (1986). A computational approach to edge detection, *IEEE Trans. Pattern Anal. Mach. Intell.* (6): 679–698.

Crook, J., Marbán, M. & Batchelar, D. (2020). Hdr prostate brachytherapy, *Semin. Radiat. Oncol.*, Vol. 30, Elsevier, pp. 49–60.

Damore, S. J., Syed, A. N., Puthawala, A. A. & Sharma, A. (2000). Needle displacement during hdr brachytherapy in the treatment of prostate cancer, *Int. J. Radiat. Oncol. Biol. Phys.* **46**(5): 1205–1211.

Fonseca, G. P., Johansen, J. G., Smith, R. L., Beaulieu, L., Beddar, S., Kertzscher, G., Verhaegen, F. & Tanderup, K. (2020). In vivo dosimetry in brachytherapy: requirements and future directions for research, development, and clinical practice, *Phys. Imaging Radiat. Oncol.* **16**: 1–11.

Fonseca, G. P., Podesta, M., Bellezzo, M., Van den Bosch, M. R., Lutgens, L., Vanneste, B. G., Voncken, R., Van Limbergen, E. J., Reniers, B. & Verhaegen, F. (2017). Online pretreatment verification of high-dose rate brachytherapy using an imaging panel, *Phys. Med. Biol.* **62**(13): 5440.

Fonseca, G. P., Viana, R. S., Podesta, M., Rubo, R. A., de Sales, C. P., Reniers, B., Yoriyaz, H. & Verhaegen, F. (2015). Hdr 192ir source speed measurements using a high speed video camera, *Med. Phys.* **42**(1): 412–415.

Gonod, M., Avila, C. C., Suarez, M. A., Crouzilles, J., Laskri, S., Vinchant, J.-F., Aubignac, L. & Grosjean, T. (2021). Miniaturized scintillator dosimeter for small field radiation therapy, *Phys. Med. Biol.* **66**(11): 115016.

Guiral, P., Ribouton, J., Jalade, P., Wang, R., Galvan, J.-M., Lu, G.-N., Pittet, P., Rivoire, A. & Gindraux, L. (2016). Design and testing of a phantom and instrumented gynecological applicator based on gan dosimeter for use in high dose rate brachytherapy quality assurance, *Med. Phys.* **43**(9): 5240–5251.

https://www.thorlabs.com/thorproduct.cfm?partnumber=DDS100/M (n.d.).

Hu, Y., Qin, Z., Ma, Y., Zhao, W., Sun, W., Zhang, D., Chen, Z., Wang, B., Tian, H. & Lewis, E. (2018a). Characterization of fiber radiation dosimeters with different embedded scintillator materials for radiotherapy applications, *Sens. Actuator A-Phys.* **269**: 188–195.

International Organization for Standardization (ISO), Guide to the Expression of Uncertainty in Measurement, International Organization for Standardization, Switzerland, 1995.

Johansen, J. G., Rylander, S., Buus, S., Bentzen, L., Hokland, S. B., Søndergaard, C. S., With, A. K. M., Kertzscher, G. & Tanderup, K. (2018). Time-resolved in vivo dosimetry for source tracking in brachytherapy, *Brachytherapy* **17**(1): 122–132.

Johansen, J., Kertzscher, G., Jørgensen, E., Rylander, S., Bentzen, L., Hokland, S., Søndergaard, C. S., With, A., Buus, S. & Tanderup, K. (2019). Dwell time verification in brachytherapy based on time resolved in vivo dosimetry, *Phys. Med.* **60**: 156–161.

Jørgensen E B *et al* 2021a A high-z inorganic scintillator–based detector for time-resolved in vivo dosimetry during brachytherapy, *Med. Phys.* **48**(11): 7382–7398.

Jørgensen E B *et al* 2021b Accuracy of an in vivo dosimetry-based source tracking method for afterloading brachytherapy—a phantom study, *Med. Phys.* **48**(5): 2614–2623.

Kertzscher, G., Andersen, C. E., Siebert, F.-A., Nielsen, S. K., Lindegaard, J. C. & Tanderup, K. (2011). Identifying afterloading pdr and hdr brachytherapy errors using real-time fiber-coupled al2o3: C dosimetry and a novel statistical error decision criterion, *Radiother. Oncol.* **100**(3): 456–462.

Kertzscher, G. & Beddar, S. (2019). Inorganic scintillation detectors for 192ir brachytherapy, *Phys. Med. Biol.* **64**(22): 225018.

Kertzscher, G., Rosenfeld, A., Beddar, S., Tanderup, K. & Cygler, J. (2014). In vivo dosimetry: trends and prospects for brachytherapy, *Brit. J. Radiol.* **87**(1041): 20140206.

Kim, Y., Hsu, I.-C., Lessard, E., Vujic, J. & Pouliot, J. (2004). Dosimetric impact of prostate volume change between ct-based hdr brachytherapy fractions, *Int. J. Radiat. Oncol. Biol. Phys.*

59(4): 1208–1216.

Kraus, J. D., Marhefka, R. J. & Khan, A. S. (2006). *Antennas and wave propagation*, Tata McGraw-Hill Education.

Lambert, J., McKenzie, D., Law, S., Elsey, J. & Suchowerska, N. (2006). A plastic scintillation dosimeter for high dose rate brachytherapy, *Phys. Med. Biol.* **51**(21): 5505.

Lambert, J., Nakano, T., Law, S., Elsey, J., McKenzie, D. R. & Suchowerska, N. (2007). In vivo dosimeters for hdr brachytherapy: a comparison of a diamond detector, mosfet, tld, and scintillation detector, *Med. Phys.* **34**(5): 1759–1765.

Linares Rosales, H. M., Archambault, L., Beddar, S. & Beaulieu, L. (2020). Dosimetric performance of a multipoint plastic scintillator dosimeter as a tool for real-time source tracking in high dose rate ir brachytherapy, *Med. Phys.* **47**(9): 4477–4490.

Linares Rosales, H. M., Duguay-Drouin, P., Archambault, L., Beddar, S. & Beaulieu, L. (2019). Optimization of a multipoint plastic scintillator dosimeter for high dose rate brachytherapy, *Med. Phys.* **46**(5): 2412–2421.

Mayadev, J., Dieterich, S., Harse, R., Lentz, S., Mathai, M., Boddu, S., Kern, M., Courquin, J. & Stern, R. L. (2015). A failure modes and effects analysis study for gynecologic high-dose-rate brachytherapy, *Brachytherapy* **14**(6): 866–875.

O'Reilly, D., Qayyum, K., Alharbi, M. & Foley, M. (2020). Temperature dependence of novel inorganic scintillation detectors, *2020 IEEE Sensors*, IEEE, pp. 1–4.

Pantelis, E., Papagiannis, P., Anagnostopoulos, G., Baltas, D., Karaiskos, P., Sandilos, P. & Sakelliou, L. (2003). Evaluation of a tg-43 compliant analytical dosimetry model in clinical 192ir hdr brachytherapy treatment planning and assessment of the significance of source position and catheter reconstruction uncertainties, *Phys. Med. Biol.* **49**(1): 55.

Perez-Calatayud, J., Ballester, F., Das, R. K., DeWerd, L. A., Ibbott, G. S., Meigooni, A. S., Ouhib, Z., Rivard, M. J., Sloboda, R. S. & Williamson, J. F. (2012). Dose calculation for photon-emitting brachytherapy sources with average energy higher than 50 kev: report of the aapm and estro, *Med. Phys.* **39**(5): 2904–2929.

Qin, Z., Hu, Y., Ma, Y., Zhao, W., Sun, W., Zhang, D., Chen, Z. & Lewis, E. (2016). Embedded structure fiber-optic radiation dosimeter for radiotherapy applications, *Opt. Express* **24**(5): 5172–5185.

Simnor, T., Li, S., Lowe, G., Ostler, P., Bryant, L., Chapman, C., Inchley, D. & Hoskin, P. J. (2009). Justification for inter-fraction correction of catheter movement in fractionated high dose-rate brachytherapy treatment of prostate cancer, *Radiother. Oncol.* **93**(2): 253–258.

Smith, R. L., Hanlon, M., Panettieri, V., Millar, J. L., Matheson, B., Haworth, A. & Franich, R. D. (2018). An integrated system for clinical treatment verification of hdr prostate brachytherapy combining source tracking with pretreatment imaging, *Brachytherapy* **17**(1): 111–121.

Suarez, M. A., Lim, T., Robillot, L., Maillot, V., Lihoreau, T., Bontemps, P., Pazart, L. & Grosjean, T. (2019). Miniaturized fiber dosimeter of medical ionizing radiations on a narrow optical fiber, *Opt. Express* **27**(24): 35588–35599.

Tanderup, K., Hellebust, T. P., Lang, S., Granfeldt, J., Pötter, R., Lindegaard, J. C. & Kirisits, C. (2008). Consequences of random and systematic reconstruction uncertainties in 3d image based brachytherapy in cervical cancer, *Radiother. Oncol.* **89**(2): 156–163.

Therriault-Proulx, F., Beddar, S. & Beaulieu, L. (n.d.). On the use of a single-fiber multipoint plastic scintillation detector for 192ir high-dose-rate brachytherapy, *Med. Phys.* **40**.

Therriault-Proulx, F., Briere, T. M., Mourtada, F., Aubin, S., Beddar, S. & Beaulieu, L. (2011). A phantom study of an in vivo dosimetry system using plastic scintillation detectors for real-time verification of 192ir hdr brachytherapy, *Med. Phys.* **38**(5): 2542–2551.

Verhaegen, F., Fonseca, G. P., Johansen, J. G., Beaulieu, L., Beddar, S., Greer, P., Jornet, N., Kertzscher, G., McCurdy, B., Smith, R. L. et al. (2020). Future directions of in vivo dosimetry for external beam radiotherapy and brachytherapy, *Phys. Imaging Radiat. Oncol.* **16**: 18–19.

Viswanathan, A. N., Beriwal, S., Jennifer, F., Demanes, D. J., Gaffney, D., Hansen, J., Jones, E.,

Kirisits, C., Thomadsen, B. & Erickson, B. (2012). American brachytherapy society consensus guidelines for locally advanced carcinoma of the cervix. part ii: high-dose-rate brachytherapy, *Brachytherapy* **11**(1): 47–52.

Wang, R., Ribouton, J., Pittet, P., Guiral, P., Jalade, P. & Lu, G.-N. (2014). Implementation of gan based real-time source position monitoring in hdr brachytherapy, *Radiat. Meas.* **71**: 293–296.